



# Rapid Ferroelectric-Photoexcited Bacteria-Killing of $\text{Bi}_4\text{Ti}_3\text{O}_{12}/\text{Ti}_3\text{C}_2\text{T}_x$ Nanofiber Membranes

Zhiying Wang<sup>1</sup> · Jianfang Li<sup>1</sup> · Yuqian Qiao<sup>2</sup> · Xiangmei Liu<sup>3</sup> · Yufeng Zheng<sup>2,5</sup> · Zhaoyang Li<sup>1</sup> · Jie Shen<sup>4</sup> · Yu Zhang<sup>5</sup> · Shengli Zhu<sup>1</sup> · Hui Jiang<sup>1</sup> · Yanqin Liang<sup>1</sup> · Zhenduo Cui<sup>1</sup> · Paul K. Chu<sup>6</sup> · Shuilin Wu<sup>1,2</sup>

Received: 1 September 2022 / Accepted: 7 November 2022 / Published online: 28 November 2022  
© Donghua University, Shanghai, China 2022

## Abstract

In this study, an antibacterial nanofiber membrane [polyvinylidene fluoride/ $\text{Bi}_4\text{Ti}_3\text{O}_{12}/\text{Ti}_3\text{C}_2\text{T}_x$  (PVDF/BTO/ $\text{Ti}_3\text{C}_2\text{T}_x$ )] is fabricated using an electrostatic spinning process, in which the self-assembled BTO/ $\text{Ti}_3\text{C}_2\text{T}_x$  heterojunction is incorporated into the PVDF matrix. Benefiting from the internal electric field induced by the spontaneously ferroelectric polarization of BTO, the photoexcited electrons and holes are driven to move in the opposite direction inside BTO, and the electrons are transferred to  $\text{Ti}_3\text{C}_2\text{T}_x$  across the Schottky interface. Thus, directed charge separation and transfer are realized through the cooperation of the two components. The recombination of electron–hole pairs is maximumly inhibited, which notably improves the yield of reactive oxygen species by enhancing photocatalytic activity. Furthermore, the nanofiber membrane with an optimal doping ratio exhibits outstanding visible light absorption and photothermal conversion performance. Ultimately, photothermal effect and ferroelectric polarization enhanced photocatalysis endow the nanofiber membrane with the ability to kill  $99.61\% \pm 0.28\%$  *Staphylococcus aureus* and  $99.71\% \pm 0.16\%$  *Escherichia coli* under 20 min of light irradiation. This study brings new insights into the design of intelligent antibacterial textiles through a ferroelectric polarization strategy.

**Keywords** Ferroelectric polarization · Antibacterial nanofiber ·  $\text{Ti}_3\text{C}_2\text{T}_x$  · Photocatalysis · Schottky heterojunction

## Introduction

Bacterial infections are the major cause of morbidity and mortality in intensive care units (ICU) worldwide [1]. They have become a threat to global public health, with multiple secondary bacterial infections [2, 3]. Since the outbreak of COVID-19 in December 2019, the course of COVID-19 patients has been complicated by bacterial infections [4, 5]. The cross-infection of bacteria also aggravates the fatality rates of COVID-19. Medical textiles, including coveralls, aprons, isolation gowns, surgical masks, and gloves [6], play an important role in protecting medical staff from external bacteria and effectively preventing cross-infection between medical workers and patients. Therefore, the demand for antibacterial textiles has dramatically increased.

The antimicrobial agents used in textiles work by either inhibiting cell growth or killing pathogens [7]. However, the long-term and systemic safety of common commercial antimicrobial agents, such as metal nanoparticles, remains a major challenge [8–10]. Therefore, various innovative antibacterial strategies are developed to rapidly eradicate bacteria, including materioherbology, photocatalytic disinfection,

✉ Shuilin Wu  
slwu@pku.edu.cn; shuilin.wu@gmail.com

<sup>1</sup> The Key Laboratory of Advanced Ceramics and Machining Technology by the Ministry of Education of China, School of Materials Science and Engineering, Tianjin University, Tianjin 300072, China

<sup>2</sup> School of Materials Science and Engineering, Peking University, Beijing 100871, China

<sup>3</sup> School of Health Science and Biomedical Engineering, Hebei University of Technology, Tianjin 300401, China

<sup>4</sup> Shenzhen Key Laboratory of Spine Surgery, Department of Spine Surgery, Peking University Shenzhen Hospital, Shenzhen 518036, China

<sup>5</sup> Department of Orthopedics, Guangdong Provincial People's Hospital, Guangdong Academy of Medical Sciences, Guangzhou 510080, China

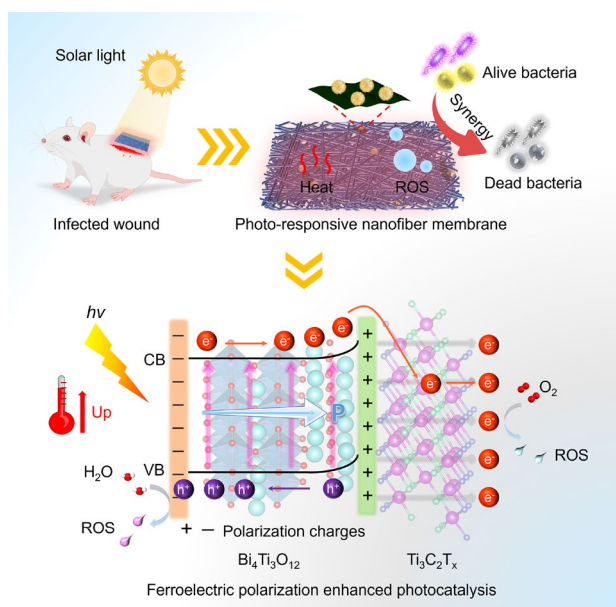
<sup>6</sup> Department of Physics, Department of Materials Science and Engineering, and Department of Biomedical Engineering, City University of Hong Kong, Hong Kong 999077, China

and photothermal therapy [11–15]. Antibacterial materials that respond to external stimuli, especially light, have been widely studied for their rapid and reusable antibacterial effect, broad antibacterial spectrum, and non-antibiotic resistance. Photo-responsive nanomaterials are excited by light with corresponding wavelengths to provide photothermal and/or photocatalytic performance with a locally increased temperature and/or reactive oxygen species (ROS) to kill bacteria [15]. Thus, the loading of photoexcited antibacterial materials on textiles can provide a new idea for designing novel antibacterial textiles.

Bismuth-based photocatalysts, such as BiOX (X = Cl, Br, I) [16] and Bi<sub>2</sub>MO<sub>6</sub> (M = W, Mo) [17] have been widely utilized for catalytic applications owing to their unique layer structure and high stability. Unlike them, Bi<sub>4</sub>Ti<sub>3</sub>O<sub>12</sub> (BTO) is a ferroelectric semiconductor with an Aurivillius phase [18]. It has a strong ferroelectric property due to its layered perovskite structure and high Curie temperature of 675 °C [19]. BTO is composed of fluorite-like [Bi<sub>2</sub>O<sub>2</sub>]<sup>2+</sup> slices and perovskite-type TiO<sub>6</sub> octahedral layers stacked along the c-axis, which form an inner electric field and promote the separation of photoexcited electrons and holes [20, 21]. The polarization effect in ferroelectric materials has been proven to be responsible for enhanced photocatalytic activity [22]. However, this activity is limited by the large bandgap and poor light absorption [18–20, 23]. Constructing heterojunctions and interface engineering can be considered an effective strategy to improve photocatalytic performance.

Ti<sub>3</sub>C<sub>2</sub>T<sub>x</sub> MXene, a typical representative material among the emerging two-dimensional layered transition metal carbides and/or nitrides family, has multiple advantages, including excellent metallic conductivity, remarkable light absorption ability, high photothermal conversion efficiency and superior biocompatibility [24, 25]. These advantages have made Ti<sub>3</sub>C<sub>2</sub>T<sub>x</sub> a promising candidate for realizing functional composite materials for wearing. In addition, Ti<sub>3</sub>C<sub>2</sub>T<sub>x</sub> has abundant surface functional groups containing F, O, and OH terminations, which can interact closely with textile substrates [26]. More importantly, it can be combined with the semiconductor of BTO to create a Schottky heterojunction. Currently, there is no literature review on BTO/Ti<sub>3</sub>C<sub>2</sub>T<sub>x</sub>, and the potential mechanism of ferro-photocatalytic sterilization is also unclear.

As a basic method for fabricating nanofibers, electrospinning is a facile and versatile technique. Electrospinning membranes have a high specific surface area, adequate mechanical strength, a complex porous structure, simple scalable fabrication, and low cost [27, 28]. Currently, more than 100 different kinds of organic polymers, such as silk fibroin, chitosan, poly(ε-caprolactone), poly(lactic acid), polystyrene, poly(vinyl chloride), polyaniline, polypyrrole, and polyvinylidene fluoride (PVDF), have been successfully electrospun into nanofibers for various applications [29].



**Scheme 1** Schematic diagram of ferroelectric polarization strategy for treating wound infection by light responsive nanofiber membrane of PVDF/BTO/Ti<sub>3</sub>C<sub>2</sub>T<sub>x</sub>

Among them, PVDF is a promising polymer matrix due to its high flexibility, ferroelectric properties, and high thermal stability [30]. Note that PVDF has a broad potential in wound dressings due to its applicability [31], anti-adhesion [32], coagulation [33], and non-neutralization with ROS [34].

Therefore, we propose the hypothesis of whether ferroelectric-photoresponsive nanofibers can be electrospun into textiles with ferroelectric polarization-strengthened photoexcited bactericidal ability to prevent pathogenic infections. To verify this, the PVDF/BTO/Ti<sub>3</sub>C<sub>2</sub>T<sub>x</sub> membrane was prepared through self-assembly and electrostatic spinning. The built-in electric field induced by the spontaneous polarization of BTO promoted the separation of charge carriers. BTO and Ti<sub>3</sub>C<sub>2</sub>T<sub>x</sub> formed a Schottky junction with a tight contact interface, in which BTO could be excited to generate electrons and holes under illumination, and electrons rapidly transferred to the side of Ti<sub>3</sub>C<sub>2</sub>T<sub>x</sub>. During light exposure, Ti<sub>3</sub>C<sub>2</sub>T<sub>x</sub> enhanced the light absorption range and photothermal conversion ability of BTO and accelerated the oriented electron transfer. The trapped electrons and holes could be used to produce more ROS (Scheme 1). Consequently, the PVDF/BTO/Ti<sub>3</sub>C<sub>2</sub>T<sub>x</sub> membrane could effectively kill pathogenic bacteria *in vitro* and *in vivo* through the synergistic effect of ROS and heat under 20 min of light irradiation.

## Experimental Section

### Preparation of BTO/Ti<sub>3</sub>C<sub>2</sub>T<sub>x</sub>

BTO nanostructures were self-assembled on Ti<sub>3</sub>C<sub>2</sub>T<sub>x</sub> nanosheets according to the following method. 80 mg of BTO was dispersed into 25 mL THF. The Ti<sub>3</sub>C<sub>2</sub>T<sub>x</sub> colloid solution with different mass ratios (20, 40, and 60 wt% of BTO) were immediately transferred to the above solution. The mixed solution was sonicated at 100 W for 4 h in an ice bath. After sonication, the solid mixtures were washed with THF for three times. The obtained materials were vacuum-dried, ground, and stored before use. These materials were named by BT20, BT40, and BT60, respectively.

### Fabrication of PVDF and PVDF/BT40 Nanofiber Membranes

All nanofiber membranes were fabricated by the electrospinning method. PVDF powder was dissolved in DMF and stirred for 1.5 h to obtain PVDF solution (18 wt%). Then different amount of BT40 (10, 30, and 50 wt% of PVDF) was added to the PVDF solution under stirring for 2.5 h. Each homogeneous mixture was poured into a syringe capped with a 21-gauge stainless steel needle, which connected with a 17 kV voltage difference. The distance between the needle tip and the collector was 15 cm. The feed rate was maintained at 1 mL h<sup>-1</sup> and the spinning time was set to 3 h. All collected nanofiber membranes were dried in the vacuum oven at 25 °C overnight. These nanofiber membranes were named PVDF, PVDF/BT40-10, PVDF/BT40-30, and PVDF/BT40-50, respectively.

### Characterization

The morphologies and microstructures of synthesized materials were observed by field emission scanning electron microscopy (FESEM, S4800, Japan) and transmission electron microscopy (TEM, JEOL JEM-2100F, Japan). The element distributions were executed by energy dispersive spectrometer (EDS, X-MAX20, UK). The phase structure was investigated by X-ray diffraction (XRD, D8 Advance, Germany). The UV–Vis–NIR absorption spectra were measured by a UV–Vis spectrophotometer (UV-2700, Shimadzu). The elemental analysis of the samples was examined by X-ray photoelectron spectroscopy (XPS, ThermoFisher Scientific 250Xi, USA). Ultraviolet photoemission spectroscopy (UPS) was conducted on an Escalab 250Xi spectrometer using He I resonance lines (21.22 eV). Photoluminescence (PL) spectra were measured by a fluorescence spectrophotometer (Fluorolog-3, USA). Raman spectroscopy was detected by a

Raman microscope (DXR2, Thermo Scientific, USA). The surface functional groups were tested by Fourier transform infrared (FTIR, Thermo Scientific Nicolet iS10, USA). The simulated sunlight came from a Xenon lamp (PLS-SXE300).

## Results and Discussion

### Synthesis and Characterization of Ti<sub>3</sub>C<sub>2</sub>T<sub>x</sub>, BTO, and BTO/Ti<sub>3</sub>C<sub>2</sub>T<sub>x</sub>

The synthesis process of the self-assembled BTO/Ti<sub>3</sub>C<sub>2</sub>T<sub>x</sub> heterostructure was shown in Fig. S1. The prepared Ti<sub>3</sub>C<sub>2</sub>T<sub>x</sub> and BTO were dispersed into tetrahydrofuran. Compared to Ti<sub>3</sub>C<sub>2</sub>T<sub>x</sub>, BTO had a small surface energy due to the presence of an oleic acid layer, resulting in good dispersibility. During the preparation, Ti<sub>3</sub>C<sub>2</sub>T<sub>x</sub> nanosheets were wrapped around the surface of the BTO nanostructure via van der Waals interactions, further minimizing the surface energy needed to form a heterostructure [35].

Ti<sub>3</sub>C<sub>2</sub>T<sub>x</sub> nanosheets were obtained from the etching and exfoliating of bulk Ti<sub>3</sub>AlC<sub>2</sub> (Fig. S2a, b). The XRD pattern of Ti<sub>3</sub>C<sub>2</sub>T<sub>x</sub> (Fig. S2c) showed a prominent diffraction peak at  $2\theta = 5.76^\circ$  corresponding to the (002) plane [36]. The wrinkled surface was characterized using TEM (Fig. S2d) to reveal the ultrathin structure of Ti<sub>3</sub>C<sub>2</sub>T<sub>x</sub> nanosheets. The high-resolution TEM (HRTEM) image (Fig. S2e) showed a corresponding lattice spacing of 0.260 nm, which was assigned to the (0  $\bar{1}$  1 0) lattice plane of Ti<sub>3</sub>C<sub>2</sub>T<sub>x</sub> [37] with a hexagonal structure in the selected area electron diffraction. Elemental mapping (Fig. S2f) showed that the Ti, C, O, and F elements were evenly distributed on the surface of Ti<sub>3</sub>C<sub>2</sub>T<sub>x</sub>.

The SEM image of BTO showed a microspherical structure composed of myriad overlapping nanosheets, with an average particle size of about 1 μm (Fig. S3a). The microstructure of the nanosheet was determined using TEM (Fig. S3b). Interplanar distances of 0.270 and 0.272 nm were indexed to (020) and (200) crystal faces, respectively (Fig. S3c) [38].

BTO/Ti<sub>3</sub>C<sub>2</sub>T<sub>x</sub> composites were labeled BT20, BT40, and BT60, and the mass of Ti<sub>3</sub>C<sub>2</sub>T<sub>x</sub> was 20, 40, and 60 wt% of BTO, respectively. SEM examination showed the morphologies of the three composites (Fig. S4a–c). The TEM and elemental mapping (Fig. 1a) showed the direct contact between Ti<sub>3</sub>C<sub>2</sub>T<sub>x</sub> and BTO. The HRTEM image (Fig. 1b) exhibited a compact interface between Ti<sub>3</sub>C<sub>2</sub>T<sub>x</sub> and BTO, as shown by the orange dashed line. The lattice fringes of 0.260, 0.270, and 0.272 nm could be attributed to the (0  $\bar{1}$  1 0), (020), and (200) faces of Ti<sub>3</sub>C<sub>2</sub>T<sub>x</sub> and BTO, respectively. The diffraction peaks of the (006), (008), (111), (115), (117), (020), (208), (220), (0214), and (137) planes of orthorhombic BTO are shown in Fig. 1c [20]. The XRD patterns of the

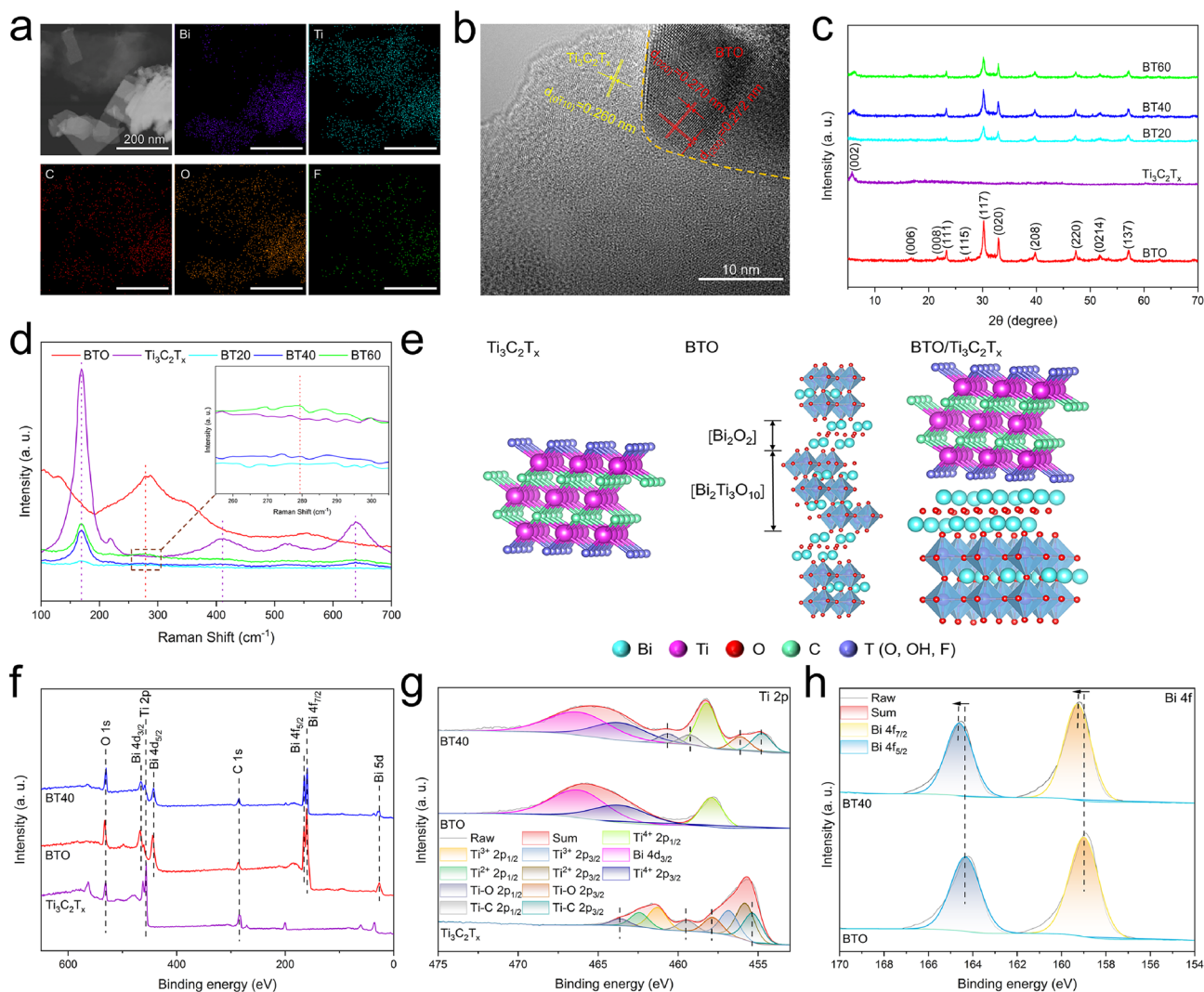


**Fig. 1** Characterization of BTO/Ti<sub>3</sub>C<sub>2</sub>T<sub>x</sub>. **a** TEM and element mapping of BT40. **b** HRTEM image of BT40. **c** XRD patterns of materials. **d** Raman spectra of materials. **e** Crystal structures of Ti<sub>3</sub>C<sub>2</sub>T<sub>x</sub>,

BTO, and BTO/Ti<sub>3</sub>C<sub>2</sub>T<sub>x</sub>. **f** The survey spectra of BTO, Ti<sub>3</sub>C<sub>2</sub>T<sub>x</sub>, and BTO/Ti<sub>3</sub>C<sub>2</sub>T<sub>x</sub>. **g** The high-resolution of Ti 2p. **h** The high-resolution of Bi 4f

BTO/Ti<sub>3</sub>C<sub>2</sub>T<sub>x</sub> composites showed the (002) peak of Ti<sub>3</sub>C<sub>2</sub>T<sub>x</sub> and all the peaks of BTO. The Raman spectra (Fig. 1d) showed that the peaks at 169 cm<sup>-1</sup> (A<sub>1g</sub>), 412 cm<sup>-1</sup> (E<sub>g</sub>), and 639 cm<sup>-1</sup> (E<sub>g</sub>) matched well with the Raman features of Ti<sub>3</sub>C<sub>2</sub>T<sub>x</sub> [39, 40], and the peaks at 250–300 cm<sup>-1</sup> represented the vibration band of the TiO<sub>6</sub> octahedron [41]. These data confirmed the combination of Ti<sub>3</sub>C<sub>2</sub>T<sub>x</sub> and BTO. The structures of BTO, Ti<sub>3</sub>C<sub>2</sub>T<sub>x</sub>, and BTO/Ti<sub>3</sub>C<sub>2</sub>T<sub>x</sub> are shown in Fig. 1e. The Aurivillius-type BTO is an asymmetric material, which can be described as (Bi<sub>2</sub>O<sub>2</sub>)<sup>2+</sup>(Bi<sub>2</sub>Ti<sub>3</sub>O<sub>10</sub>)<sup>2-</sup>. Ti<sub>3</sub>C<sub>2</sub>T<sub>x</sub> provided surface termination groups, resulting in abundant active sites on the surface and promoting the combination with BTO.

The chemical states of the elements of Ti<sub>3</sub>C<sub>2</sub>T<sub>x</sub>, BTO, and BTO/Ti<sub>3</sub>C<sub>2</sub>T<sub>x</sub> were obtained using XPS (Fig. 1f–h and

Fig. S5). All spectra were calibrated by the C 1s peak at 284.8 eV. The elements of Bi, Ti, C, and O co-existed in BTO/Ti<sub>3</sub>C<sub>2</sub>T<sub>x</sub> (Fig. 1f), suggesting a successful combination of BTO and Ti<sub>3</sub>C<sub>2</sub>T<sub>x</sub>. As shown in Fig. 1g, the Ti 2p spectra in Ti<sub>3</sub>C<sub>2</sub>T<sub>x</sub> could be deconvoluted into eight peaks of Ti–C, Ti<sup>2+</sup>, Ti<sup>3+</sup>, and Ti–O [42]. BTO/Ti<sub>3</sub>C<sub>2</sub>T<sub>x</sub> only showed peaks of Ti–O and Ti–C, and the binding energies shifted to lower positions compared to those of Ti<sub>3</sub>C<sub>2</sub>T<sub>x</sub>, consistent with the binding energy change in the Ti–C peak in the C 1s spectra (Fig. S5a). The Ti 2p profiles in both BTO and BTO/Ti<sub>3</sub>C<sub>2</sub>T<sub>x</sub> partially overlapped with those of Bi 4d<sub>3/2</sub> at 466.4 eV. For the Bi 4f spectra (Fig. 1h), two main peaks at 158.9 and 164.3 eV in pure BTO were specified as Bi 4f<sub>7/2</sub> and Bi 4f<sub>5/2</sub> of Bi<sup>3+</sup> [38], while they became 159.2 and 164.6 eV in BTO/Ti<sub>3</sub>C<sub>2</sub>T<sub>x</sub>, respectively. This proved that the electron density



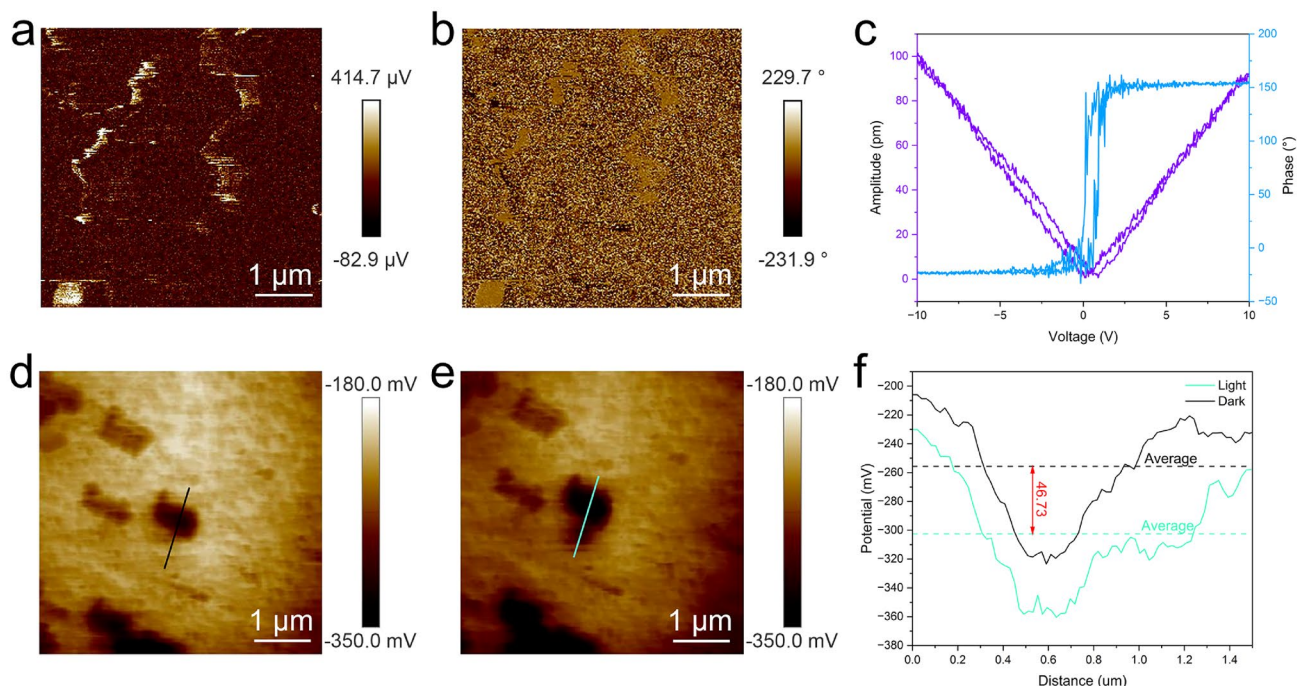


**Fig. 2** Ferroelectric property of BTO/Ti<sub>3</sub>C<sub>2</sub>T<sub>x</sub>. **a** PFM amplitude image. **b** PFM phase image. **c** Amplitude-voltage curve and phase-voltage curve of BTO/Ti<sub>3</sub>C<sub>2</sub>T<sub>x</sub>. **d** KPFM image in the dark. **e** KPFM

image under illumination. **f** Surface potential distribution of BTO/Ti<sub>3</sub>C<sub>2</sub>T<sub>x</sub> on the selected line under dark (black) and light (cyan)

of Bi in BTO/Ti<sub>3</sub>C<sub>2</sub>T<sub>x</sub> decreased due to the strong interaction between BTO and Ti<sub>3</sub>C<sub>2</sub>T<sub>x</sub>. The O 1s (Fig. S5b) and F 1s spectra (Fig. S5c) showed the peaks of the surface oxygen substances in BTO/Ti<sub>3</sub>C<sub>2</sub>T<sub>x</sub> and the surface terminal group of F in Ti<sub>3</sub>C<sub>2</sub>T<sub>x</sub>. These results confirmed that the interfacial electrons were transferred from BTO to Ti<sub>3</sub>C<sub>2</sub>T<sub>x</sub> due to the strong interface interaction between BTO and Ti<sub>3</sub>C<sub>2</sub>T<sub>x</sub>, which led to the formation of the Schottky heterojunction of BTO/Ti<sub>3</sub>C<sub>2</sub>T<sub>x</sub>.

### Ferroelectric Property and Photocatalytic Performance of BTO/Ti<sub>3</sub>C<sub>2</sub>T<sub>x</sub>

Ferroelectricity was characterized using a piezo-response force microscope (PFM) and Kelvin probe force microscopy (KPFM). Figure 2a, b showed the PFM amplitude image and phase image of BTO/Ti<sub>3</sub>C<sub>2</sub>T<sub>x</sub>. The typical amplitude voltage butterfly loops and well-defined 180° phase reversal hysteresis loops were obtained under the ±10 V DC bias field, confirming the ferroelectric feature of BTO/Ti<sub>3</sub>C<sub>2</sub>T<sub>x</sub> (Fig. 2c). The KPFM images under dark and light conditions were shown in Fig. 2d, e. The surface potential with illumination was lower than that without illumination. This could be interpreted as more photogenerated carriers migrating in the opposite direction under illumination driven by the potential difference. The difference in surface potential between dark and light was 46.73 mV (Fig. 2f), indicating

that the polarization electric field was conducive to promoting the separation and migration of photogenerated carriers.

To investigate the effect of ferroelectric polarization on photogenerated charge migration, the photoelectrochemical properties were measured. As shown in Fig. 3a, the photocurrent density of BTO/Ti<sub>3</sub>C<sub>2</sub>T<sub>x</sub> hybrids was much larger than that of individual BTO and Ti<sub>3</sub>C<sub>2</sub>T<sub>x</sub>, indicating that more free electrons were transferred under illumination. BT40 had the highest photocurrent density. Furthermore, BT40 had the smallest semicircle radius (Fig. 3b), demonstrating the lowest electrical impedance. Thus, BT40 had the best photoelectric performance, which was ascribed to the optimal doping amount of Ti<sub>3</sub>C<sub>2</sub>T<sub>x</sub>. The effective interfacial transfer of photogenerated charges was realized using the most compact interface between BTO and Ti<sub>3</sub>C<sub>2</sub>T<sub>x</sub> [43]. Conversely, BTO presented great resistance to electron transfer in darkness, proving that spontaneous polarization alone could not rapidly migrate electrons. These results showed the efficient separation of photogenerated charges under the synergy of spontaneous polarization and Schottky heterojunction. Furthermore, the peak intensity of BT40 in the PL spectra (Fig. 3c) was obviously lower than that of BTO, implying that the recombination of photoexcited carriers was greatly restrained. The separated electrons and holes were captured by the surrounding oxygen species to produce ROS, which were detected using electron spin resonance (ESR). No obvious signs of hydroxyl radical

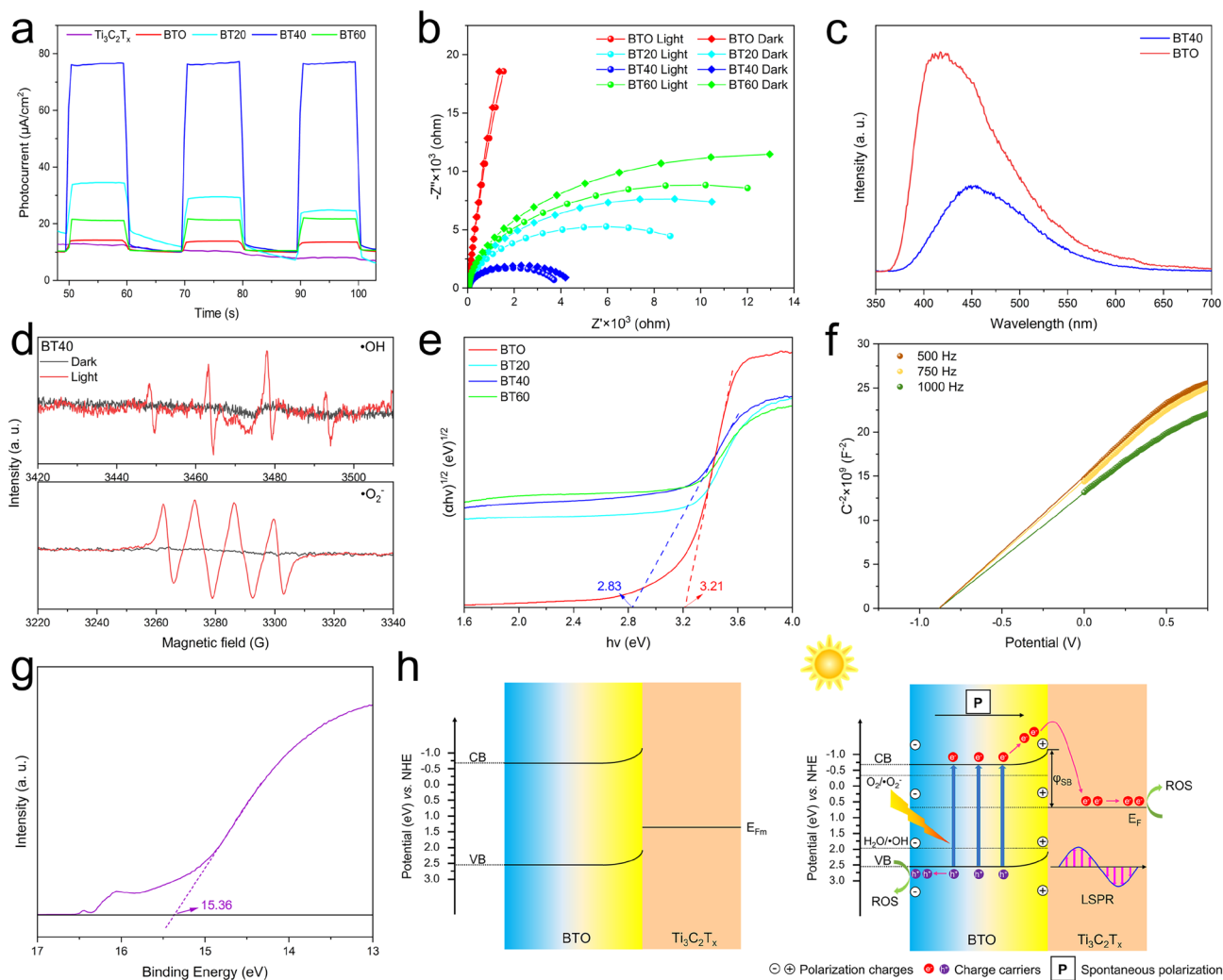


**Fig. 3** Photocatalytic performance of BTO/Ti<sub>3</sub>C<sub>2</sub>T<sub>x</sub> and the mechanism of ferroelectric polarization enhanced photocatalysis. **a** Photocurrent response under illumination. **b** EIS spectra with or without light. **c** Steady-state PL spectra of BT40 and BTO. **d** ESR spectra of ·OH and ·O<sub>2</sub><sup>-</sup>. **e** The bandgap of BTO, BT20, BT40, and BT60. **f**

Mott–Schottky curves of BTO at different frequencies. **g** Secondary electron cutoff of Ti<sub>3</sub>C<sub>2</sub>T<sub>x</sub>. **h** Energy band structure diagram before illumination and charge directed migration and ROS production mechanism under illumination

(·OH) or superoxide radical (·O<sub>2</sub><sup>-</sup>) were detected without light (Fig. 3d). Under illumination, the characteristic peaks of ·OH and ·O<sub>2</sub><sup>-</sup> occurred, indicating the production of ·OH and ·O<sub>2</sub><sup>-</sup>. This result confirmed the efficient separation and transfer of photogenerated carriers in BT40 under illumination, which was consistent with the photocurrent results (Fig. 3a).

In addition, the photothermal ability of the materials was tested under Xenon lamp irradiation (0.15 W cm<sup>-2</sup>) for 15 min (Fig. S6). Ti<sub>3</sub>C<sub>2</sub>T<sub>x</sub> exhibited an excellent photothermal effect, with the highest temperature of 59.4 °C, which could be attributed to its localized surface plasmon resonance (LSPR) effect [44]. However, pure BTO only increased from 29.1 to 49.7 °C, which was almost the same as the Control group. The temperatures of BT20, BT40, and

BT60 were 56.9, 58.1, and 57.4 °C, respectively, which were significantly higher than that of BTO. Compared to BT20 and BT60, BT40 had the highest temperature. This proved that the moderate addition of Ti<sub>3</sub>C<sub>2</sub>T<sub>x</sub> could effectively improve the photothermal effect of BTO.

Compared to BTO, the photo-responsive range and photothermal conversion efficiency of BTO/Ti<sub>3</sub>C<sub>2</sub>T<sub>x</sub> was enlarged (Fig. S7, 8), indicating the good light absorption of the composites under visible light. The energy gap (*E<sub>g</sub>*) was estimated in the Tauc plot (Fig. 3e). The bandgap of BTO was 3.21 eV, whereas BT40 exhibited a narrower bandgap of 2.83 eV. The Mott–Schottky plot (Fig. 3f) showed that BTO was an n-type semiconductor with a flat band potential (*E<sub>fb</sub>*) of -0.88 eV. Thus, the conduction band (CB) and valence band (VB) of BTO was -0.68 and 2.53 eV, respectively.

As shown in Fig. 3g, the secondary electron cutoff edge of  $\text{Ti}_3\text{C}_2\text{T}_x$  was 15.36 eV, and the corresponding work function ( $W_F$ ) was 5.86 eV, which was determined by subtracting from the excitation energy of He I (21.20 eV). The Fermi level ( $E_F$ ) of BTO was reported to be  $-0.088$  eV [23]. The band structure diagram of BTO/ $\text{Ti}_3\text{C}_2\text{T}_x$  was shown in Fig. 3h (left). As the  $W_F$  of  $\text{Ti}_3\text{C}_2\text{T}_x$  was higher than that of BTO, a Schottky heterojunction was formed when BTO came into contact with  $\text{Ti}_3\text{C}_2\text{T}_x$ . The electrons were transferred from BTO to  $\text{Ti}_3\text{C}_2\text{T}_x$  until the  $E_F$  reached equilibrium, accompanied by an upward bending of the energy band of BTO and the formation of the Schottky barrier ( $\varphi_{SB}$ ).

The mechanism of the enhanced photocatalytic activity is shown in Fig. 3h (right). Upon visible light irradiation, electrons transitioned from VB to CB of BTO. Spontaneous polarization arose from the distortion of the  $[\text{TiO}_6]$  octahedra of ferroelectric BTO [38]. Photogenerated carriers were diffused in the opposite direction under the internal electric field induced by the polarization charges. Thus, more photoelectrons crossed the  $\varphi_{SB}$  into  $E_F$  of  $\text{Ti}_3\text{C}_2\text{T}_x$ . The  $\varphi_{SB}$  inhibited the backflow of electrons, which efficiently prohibited the recombination of electrons and holes. The photoinduced electrons directionally migrated to  $\text{Ti}_3\text{C}_2\text{T}_x$ , and holes were trapped in BTO. Additionally,  $\text{Ti}_3\text{C}_2\text{T}_x$  endowed BTO with a wider light response range. The increased light absorption excited more photogenerated carriers. The charge carriers rapidly reacted with  $\text{O}_2$  and  $\text{H}_2\text{O}$  to produce abundant ROS in  $\text{Ti}_3\text{C}_2\text{T}_x$  and BTO, respectively. In sum, ferroelectric polarization promoted the directional separation and transfer of charge carriers, reduced the recombination of carriers, and further improved photocatalytic performance.

### BT40-Based Light-Responsive Antibacterial Nanofiber Membrane

Based on the optimal light response, antibacterial property, and biocompatibility (Fig. 3a, b and Fig. S9, 10), BT40 was used in electrostatic spinning to design smart antibacterial textiles for killing pathogenic bacteria. The preparation of the electrospinning nanofiber membrane is illustrated in Fig. 4a. BT40 was integrated into PVDF through electrospinning with different percentages (i.e., 0, 10, 30, and 50 wt%), forming PVDF/BT40 composite membranes. The SEM images and photographs of PVDF, PVDF/BT40-10, PVDF/BT40-30, and PVDF/BT40-50 were shown in Fig. 4b–e. A pure PVDF membrane was composed of uniformly distributed nanofibers with a diameter of about 300 nm. The spheres in PVDF/BT40-50 contained Bi, Ti, and O elements, identified as BTO (Fig. S11). However, the  $\text{Ti}_3\text{C}_2\text{T}_x$  nanosheets were dissolved in the solvent during the preparation of the mixed electrospinning solution, which could be the reason for the improved tensile property of composite membranes. BT40 was both aggregated

and partially dispersed in the PVDF matrix, and both states could respond to light. The FTIR spectra (Fig. S12) showed absorption bands at 840 and 1180  $\text{cm}^{-1}$ , which corresponded to the  $\beta$ -crystal phase of PVDF. PVDF/BT40 membranes had similar peaks to pristine PVDF membranes, indicating that the BT40 filler had no significant effect on the crystal phase of the PVDF substrate.

The hydrophobicity, flexibility, and breathability of the nanofiber membranes were also investigated. The contact angles of PVDF, PVDF/BT40-10, PVDF/BT40-30, and PVDF/BT40-50 were 139°, 143°, 141.7°, and 140.4°, respectively (Fig. 4f). They were far larger than 90°, demonstrating their remarkable hydrophobicity. The tensile strength of PVDF/BT40 membranes was greater than that of the pure PVDF membranes (Fig. 4g). The improved strength was attributed to the reinforcement of  $\text{Ti}_3\text{C}_2\text{T}_x$  in BT40 phase. However, the tensile strength of PVDF/BT40-60 decreased due to the excessive doping amount of BT40. The photographs of bend and torsion imply the flexibility of PVDF/BT40-50. Furthermore, the stability of BT40 in the membranes before and after stretching was characterized using XRD (Fig. S13). These results suggested that the PVDF/BT40-50 had enough strength and stability to be woven into textiles. The white smoke produced by volatile HCl and  $\text{NH}_3 \cdot \text{H}_2\text{O}$  indicated the good air permeability of PVDF/BT40-50 (Fig. 4h). Moreover, the water vapor transmittance rate (WVTR) was tested under the ASTM E96 inverse cup standard [45]. The WVTR of PVDF, PVDF/BT40-10, PVDF/BT40-30, and PVDF/BT40-50 was 66, 77, 82, and 92  $\text{g m}^{-2} \text{h}^{-1}$  (Fig. 4i). This showed that the air permeability of PVDF/BT40 membranes was improved, which arose from the increase of inter-fiber pore size after doping BT40 [46]. The best air permeability of PVDF/BT40-50 implied good comfort when attached to human skin.

The UV–Vis–NIR absorption spectra showed that the light absorption intensity was enhanced with the doping of BT40 (Fig. 4j). The temperature changes in the nanofiber membranes under illumination (0.1  $\text{W cm}^{-2}$ , 20 min) were recorded to assess the photothermal effect (Fig. 4k and Fig. S14a). The temperature of PVDF/BT40 membranes was higher than that of PVDF, indicating a better photothermal conversion ability. PVDF/BT40-50 presented repeatable temperature changes after three cycles, proving its excellent photothermal stability (Fig. S14b). Moreover, the temperature remained almost constant after five washing cycles, indicating the photothermal durability of PVDF/BT40-50 (Fig. S14c). The photothermal conversion efficiencies of PVDF/BTO, PVDF/ $\text{Ti}_3\text{C}_2\text{T}_x$ , and PVDF/BT40-50 were calculated in Fig. S15. The ROS generation ability of PVDF/BT40-50 was confirmed by the ESR spectra (Fig. 4l, m). The results showed that PVDF/BT40-50 could produce  $\cdot\text{OH}$  and  $\cdot\text{O}_2^-$  under visible light irradiation. For the photocatalytic properties of all membranes, rhodamine B photodegradation



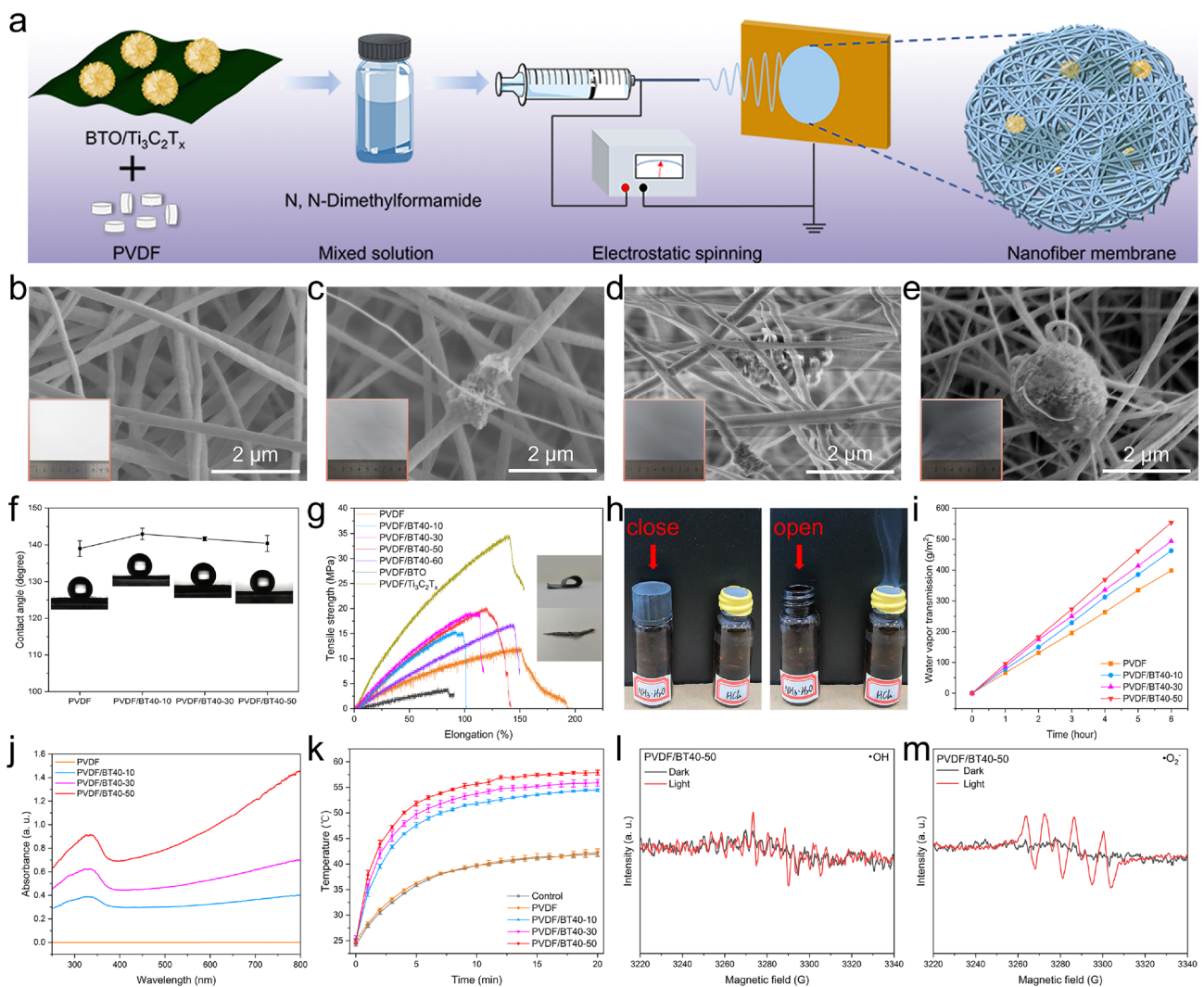


**Fig. 4** Synthesis, characterization, and properties of nanofiber membranes. **a** The schematic diagram of synthesis of electrospinning nanofiber membrane. **b–e** SEM images of PVDF (**b**), PVDF/BT40-10 (**c**), PVDF/BT40-30 (**d**), PVDF/BT40-50 (**e**), and insets show the photographs of the nanofiber membranes. **f** Digital images of contact angles of water droplets on the surface of nanofiber membranes. **g** Mechanical tests of the tensile strength *versus* elongation and inset

shows the photograph of bend and torsion of PVDF/BT40-50. **h** Digital photographs of gas permeability of PVDF/BT40-50. **i** Water vapor transmittance rate. **j** UV–Vis–NIR absorption spectra of membranes from 250 to 800 nm. **k** Photothermal curves of different membranes under light irradiation ( $0.1 \text{ W cm}^{-2}$ , 20 min). **l** ESR spectra of  $\cdot\text{OH}$ . **m** ESR spectra of  $\cdot\text{O}_2^-$

was performed (Fig. S16). The degradation of PVDF/BT40-60 was not greater than that of PVDF/BT40-50, which proved that 50 wt% of BT40 was the best doping amount.

### Antibacterial Activity Test and Biosafety Evaluation

Representative Gram-positive *Staphylococcus aureus* and Gram-negative *Escherichia coli* were chosen as the experimental strains to evaluate the antibacterial performance of nanofiber membranes. Antibacterial activity was determined using the spread plate method under simulated sunlight irradiation with an air mass 1.5 (AM 1.5) filter. After treatment

with simulated sunlight ( $0.1 \text{ W cm}^{-2}$ , 20 min), the antibacterial effect of the PVDF/BT40 membrane was particularly significant, with dramatically reduced bacterial counts, while the colonies of *S. aureus* or *E. coli* of all groups almost had no variation without illumination (Fig. 5a, b). The antibacterial rates of PVDF/BT40-50 against *S. aureus* and *E. coli* were  $99.61\% \pm 0.28\%$  and  $99.71\% \pm 0.16\%$ , respectively (Fig. 5c, d). This implied that PVDF/BT40-50 had highly effective and broad-spectrum antibacterial activity. The fast bacteria-killing behavior of the materials and composite membrane was superior to other works [47–49]. However, due to excessive doping of BT40, the antibacterial effect



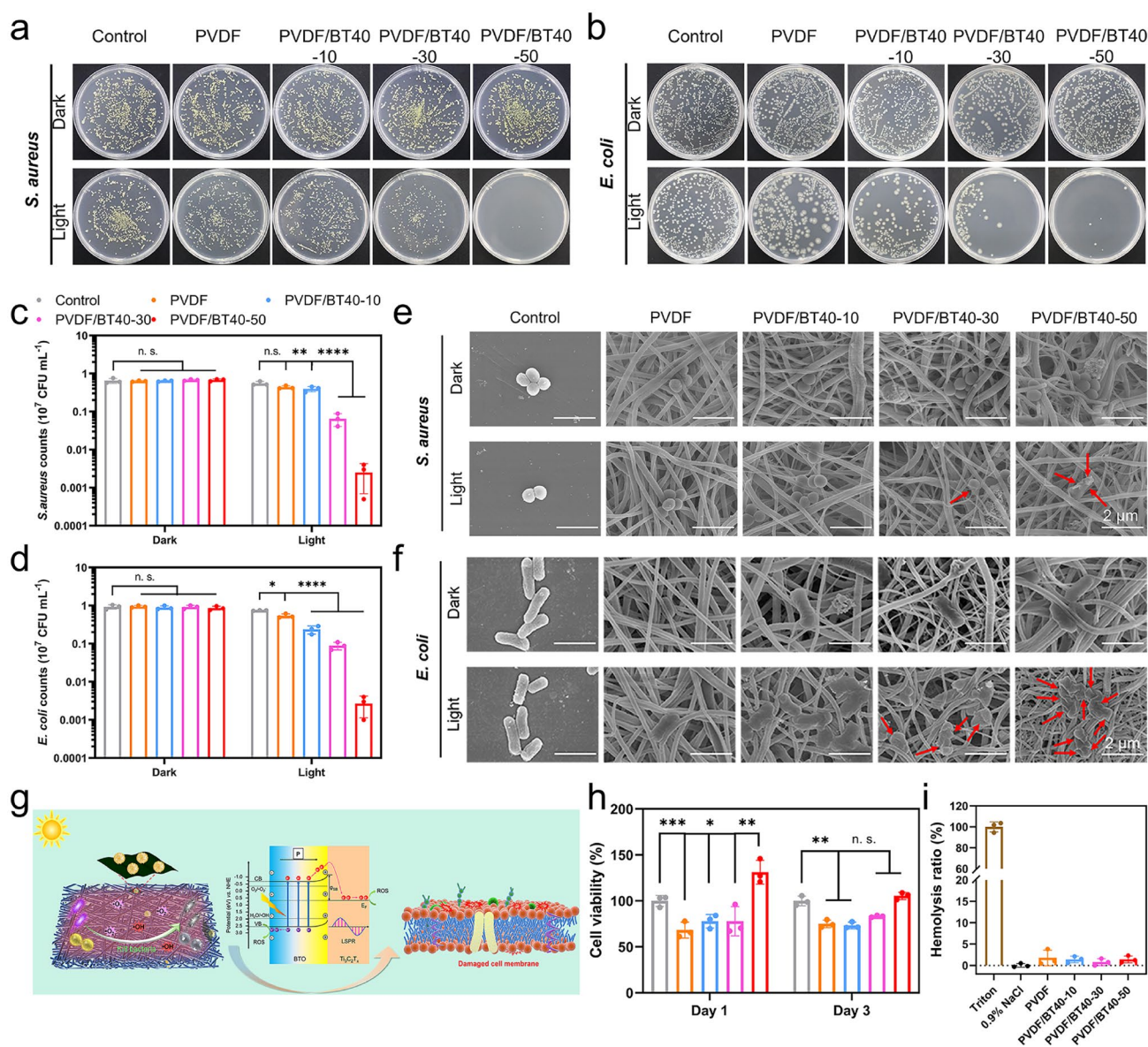


**Fig. 5** Antibacterial performance and biocompatibility of nanofiber membranes. **a, b** Spread plates of *S. aureus* (**a**) and *E. coli* (**b**) treated with Control, PVDF, PVDF/BT40-10, PVDF/BT40-30, and PVDF/BT40-50 without and with illumination ( $0.1 \text{ W cm}^{-2}$ ) for 20 min. **c, d** The corresponding statistical chart of strain counts of *S. aureus* (**c**)

and *E. coli* (**d**). **e, f** The morphologies of *S. aureus* (**e**) and *E. coli* (**f**) in the dark and light. **g** Schematic diagram of antibacterial mechanism of nanofiber membrane. **h** Cell viability of nanofiber membranes after coculturing for 1 and 3 days. **i** Hemolysis ratio of different membranes. \* $P < 0.05$ , \*\* $P < 0.01$ , \*\*\* $P < 0.001$ , \*\*\*\* $P < 0.0001$

of PVDF/BT40-60 was not further improved (Fig. S17). Therefore, PVDF/BT40-50 had the best antibacterial activity. The excellent antibacterial activity could be derived from the synergistic effect of combining ROS and hyperthermia induced by light irradiation. To explain the antibacterial mechanism, the bacterial morphologies in the different membranes were observed using SEM (Fig. 5e, f). Under illumination, the morphologies of both *S. aureus* and *E. coli* in the PVDF/BT40 group were differently destroyed with plicated and broken membranes (red arrows), whereas the

PVDF and Control groups showed intact membranes and smooth surfaces. More severe damage was found in PVDF/BT40-50. This result further verified that PVDF/BT40-50 had high-efficiency antibacterial activity under illumination, consistent with the spread plate results.

Figure 5g shows the antibacterial mechanism of the nanofiber membrane. When contacting the membrane, the bacteria were killed by ROS and heat under light. That is, the BT40 composites on the surface of the nanofiber membrane responded to visible light and photogenerated carriers were



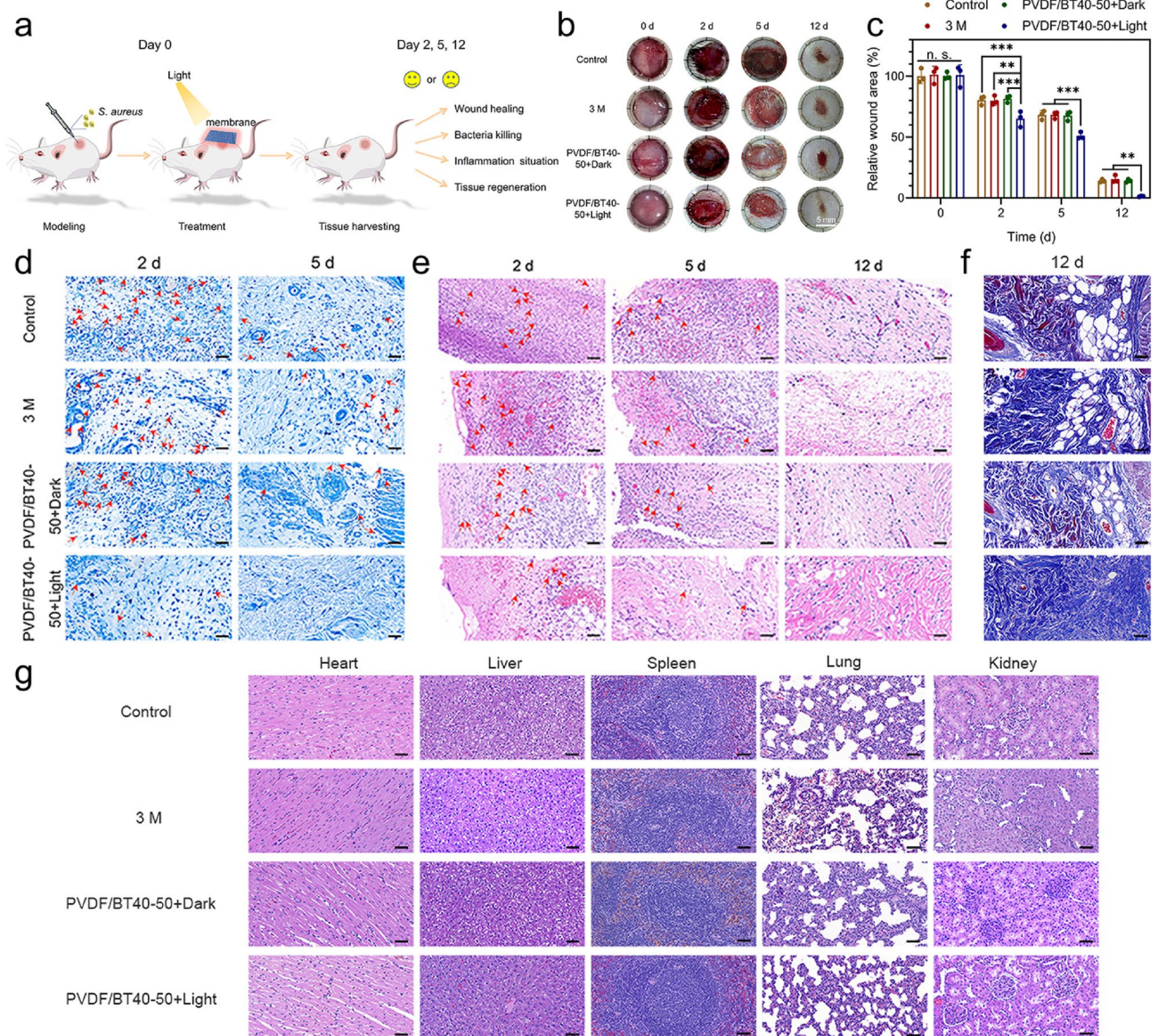


**Fig. 6** Antibacterial assay in vivo. **a** The flow chart of animal experiments. **b, c** The actual images (**b**) and area statistics (**c**) of the infected wounds on 0, 2, 5, and 12 days for Control, 3 M, PVDF/BT40-50+Dark, and PVDF/BT40-50+Light. **d** Giemsa staining for infected wound tissues collected on 2 and 5 days. Scale bars: 50  $\mu$ m. **e** H&E staining of infected tissues after 2, 5, and 12 days of treat-

ment. Scale bars: 50  $\mu$ m. **f** Masson staining on 12 days. Scale bars: 50  $\mu$ m. **g** H&E staining of the heart, liver, spleen, lung, and kidney tissues. Scale bars: 50  $\mu$ m. \* $P$  < 0.05, \*\* $P$  < 0.01, \*\*\* $P$  < 0.001, \*\*\*\* $P$  < 0.0001. (Bacteria and neutrophils were labeled by red arrows in **d** and **e**)

excited in the semiconductor BTO. The inner electric field induced by the polarization charge of the BTO facilitated the separation and transfer of electrons and holes. Due to the formation of the Schottky heterojunction of BTO/ $\text{Ti}_3\text{C}_2\text{T}_x$ , the photoexcited electrons were transferred from BTO to  $\text{Ti}_3\text{C}_2\text{T}_x$  to generate ROS. Simultaneously, the photothermal effect was activated in BTO/ $\text{Ti}_3\text{C}_2\text{T}_x$  to produce heat. Based on ROS and heat, the cell membranes of the bacteria were damaged. The bacteria were sensitive to heat under the attack of ROS. Heat increased the permeability of the cell

membrane, allowing ROS to enter the cell membrane more easily. Thus, the ROS and heat were synergetic in destroying the structure of bacteria and achieving the purpose of sterilization.

The cell viability assay of nanofiber membranes was performed using a Cell Counting Kit 8 (CCK-8). NIH-3T3 cells were incubated with different membranes for one and three days, and the results showed that the cell activity increased with the doping content of BT40 (Fig. 5h). After one day, PVDF/BT40-50 could promote cell proliferation compared

to the Control group. After three days, all groups showed no obvious cytotoxicity. In addition, the hemolysis rates of PVDF, PVDF/BT40-10, PVDF/BT40-30, and PVDF/BT40-50 were lower than 5% (Fig. 5i), revealing that the fabricated nanofiber membranes had good blood compatibility and biological safety in vivo.

### In Vivo Wound Infection Treatment with PVDF/BT40-50

A model rat skin wound, infected with *S. aureus* was developed to evaluate the therapeutic effects of PVDF/BT40-50 in vivo, as shown in Fig. 6a. The thermal images of PVDF/BT40-50 + Light group under illumination for 20 min were recorded in Fig. S18. The wound of the PVDF/BT40-50 + Light group was almost completely healed after 12 days, whereas the wounds of the Control, 3 M, and PVDF/BT40-50 + Dark groups still did not coalesce (Fig. 6b). The statistics of wound areas showed that PVDF/BT40-50 + Light group had the best therapeutic efficacy (Fig. 6c). After two and five days of treatment, the number of bacteria in the infected tissue was visibly reduced after PVDF/BT40-50 + Light treatment (Fig. 6d). Hematoxylin and eosin (H&E) staining showed that the number of neutrophils in PVDF/BT40-50 + Light group was significantly lower than that in the other groups, reflecting the minimum level of inflammation (Fig. 6e). The above data suggested that PVDF/BT40-50 had an excellent antibacterial effect irradiated by light and showed good application prospects in the treatment of tissue infection. Moreover, the area of collagen fibers in the PVDF/BT40-50 + Light group was highest (Fig. 6f), showing strong tissue regeneration ability and promoting wound healing ability. The heart, liver, spleen, lung, and kidney of the rats were analyzed using H&E staining (Fig. 6g). No abnormality was observed in the main organs, indicating that PVDF/BT40-50 was biosafe in vivo.

### Conclusions

In summary, the self-assembled BTO/Ti<sub>3</sub>C<sub>2</sub>T<sub>x</sub> heterostructure was successfully constructed and embedded into the nanofibers through electrospinning. The PVDF/BT40-50 nanofiber membrane had prominent hydrophobicity, flexibility, and permeability, meeting the requirements of wearability. The spontaneous polarization of ferroelectric BTO first separated the inner photogenerated electrons and holes, and then the electrons migrated to Ti<sub>3</sub>C<sub>2</sub>T<sub>x</sub> under the Schottky heterojunction of BTO/Ti<sub>3</sub>C<sub>2</sub>T<sub>x</sub>. The charge carriers were reversely separated and utilized to the maximum extent, thus boosting the improvement in photocatalytic ability. Combining the generated ROS and heat, the PVDF/

BT40-50 membrane exhibited high-efficiency antibacterial efficacies of 99.61% ± 0.28% and 99.71% ± 0.16% against *S. aureus* and *E. coli* under simulated solar light irradiation for 20 min, respectively. Moreover, the membrane showed good biocompatibility and strong wound healing ability. This study provides new insights into developing smart functional textiles incorporated with light-responsive antibacterial nanomaterials.

**Supplementary Information** The online version contains supplementary material available at <https://doi.org/10.1007/s42765-022-00234-8>.

**Acknowledgements** This work is jointly supported by the National Natural Science Foundation of China (Nos. 51871162, 52173251, 82002303), the China National Funds for Distinguished Young Scholars (No. 51925104), the Central Guidance on Local Science and Technology Development Fund of Hebei Province (226Z1303G), Scientific Research Foundation of Peking University Shenzhen Hospital (KYQD2021064), Guangdong Basic and Applied Basic Research Foundation (2021A1515220093, 2022A1515011536) and NSFC-Guangdong Province Joint Program (Key program no. U21A2084).

### Declarations

**Conflict of interest** The authors declare no competing financial interest.

### References

1. Vincent JL, Rello J, Marshall J, Silva E, Anzueto A, Martin CD, Moreno R, Lipman J, Gomersall C, Sakr Y, Reinhart K. International study of the prevalence and outcomes of infection in intensive care units. *J Am Med Assoc* **2009**;302:2323.
2. Nelson RE, Hatfield KM, Wolford H, Samore MH, Scott RD, Reddy SC, Olubajo B, Paul P, Jernigan JA, Baggs J. National estimates of healthcare costs associated with multidrug-resistant bacterial infections among hospitalized patients in the United States. *Clin Infect Dis* **2021**;72:S17.
3. Jernigan JA, Hatfield KM, Wolford H, Nelson RE, Olubajo B, Reddy SC, McCarthy N, Paul P, McDonald LC, Kallen A, Fiore A, Craig M, Baggs J. Multidrug-resistant bacterial infections in US hospitalized patients, 2012–2017. *N Engl J Med* **2020**;382:1309.
4. Moore JB, June CH. Cytokine release syndrome in severe COVID-19. *Science* **2020**;368:473.
5. Moreno-Torres V, de Mendoza C, de la Fuente S, Sanchez E, Martinez-Urbistondo M, Herraiz J, Gutierrez A, Gutierrez A, Hernandez C, Callejas A, Mainez C, Royuela A, Cuervas-Mons V. Bacterial infections in patients hospitalized with COVID-19. *Intern Emerg Med* **2021**;17:431.
6. CDC. Personal protective equipment (PPE). 2020. <https://www.cdc.gov/coronavirus/2019-ncov/hcp/using-ppe.html>. Accessed 19 Aug 2020.
7. Karim N, Afroj S, Lloyd K, Oaten LC, Andreeva DV, Carr C, Farmery AD, Kim ID, Novoselov KS. Sustainable personal protective clothing for healthcare applications: a review. *ACS Nano* **2020**;14:12313.
8. Makabenta JMV, Nabawy A, Li CH, Schmidt-Malan S, Patel R, Rotello VM. Nanomaterial-based therapeutics for antibiotic-resistant bacterial infections. *Nat Rev Microbiol* **2021**;19:23.



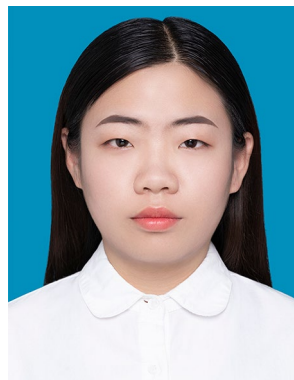
9. Matatkova O, Michailidu J, Miskovska A, Kolouchova I, Masak J, Cejkova A. Antimicrobial properties and applications of metal nanoparticles biosynthesized by green methods. *Biotechnol Adv* **2022**;58:107905.
10. Guo ZC, Chen Y, Wang YH, Jiang H, Wang XM. Advances and challenges in metallic nanomaterial synthesis and antibacterial applications. *J Mater Chem B* **2020**;8:4764.
11. Zhou ZA, Li J, Tan L, Liu XM, Zheng YF, Cui ZD, Li CY, Yeung KWK, Li ZY, Liang YQ, Zhu SL, Wu SL. Using tea nanoclusters as  $\beta$ -lactamase inhibitors to cure multidrug-resistant bacterial pneumonia: a promising therapeutic strategy by Chinese materio-herbology. *Fundam Res* **2022**;2:496.
12. Li J, Zhou ZA, Liu XM, Zheng YF, Li CY, Cui ZD, Yeung KWK, Zhou HB, Zou JH, Li ZY, Zhu SL, Liang YQ, Wang XB, Wu SL. Material-herbology: an effective and safe strategy to eradicate lethal viral-bacterial pneumonia. *Matter* **2021**;4:3030.
13. Qiao YQ, Xu YD, Liu XM, Zheng YF, Li B, Han Y, Li ZY, Yeung KWK, Liang YQ, Zhu SL, Cui ZD, Wu SL. Microwave assisted antibacterial action of garcinia nanoparticles on gram-negative bacteria. *Nat Commun* **2022**;13:2461.
14. Jin LG, Liu XM, Zheng YF, Li ZY, Zhang Y, Zhu SL, Jiang H, Cui ZD, Chu PK, Wu SL. Interface polarization strengthened microwave catalysis of  $\text{MoS}_2/\text{FeS}/\text{Rhein}$  for the therapy of bacteria-infected osteomyelitis. *Adv Funct Mater* **2022**;32:2204437.
15. Liu HP, Li JF, Liu XM, Li ZY, Zhang Y, Liang YQ, Zheng YF, Zhu SL, Cui ZD, Wu SL. Photo-sono interfacial engineering exciting the intrinsic property of herbal nanomedicine for rapid broad-spectrum bacteria killing. *ACS Nano* **2021**;15:18505.
16. Guo JY, Li X, Liang J, Yuan XZ, Jiang LB, Yu HB, Sun HB, Zhu ZQ, Ye SJ, Tang N, Zhang J. Fabrication and regulation of vacancy-mediated bismuth oxyhalide towards photocatalytic application: development status and tendency. *Coordin Chem Rev* **2021**;443:214033.
17. Li HP, Hou WG, Tao XT, Du N. Conjugated polyene-modified  $\text{Bi}_2\text{MO}_6$  ( $\text{M}=\text{Mo}$  or  $\text{W}$ ) for enhancing visible light photocatalytic activity. *Appl Catal B Environ* **2015**;172:27.
18. Das K, Majhi D, Bhoi YP, Mishra BG. Combustion synthesis, characterization and photocatalytic application of  $\text{CuS}/\text{Bi}_4\text{Ti}_3\text{O}_{12}$  p-n heterojunction materials towards efficient degradation of 2-methyl-4-chlorophenoxyacetic acid herbicide under visible light. *Chem Eng J* **2019**;362:588.
19. Zhang Q, Shi YY, Shi XJ, Huang TT, Lee SC, Huang Y, Cao JJ. Constructing Pd/ferroelectric  $\text{Bi}_4\text{Ti}_3\text{O}_{12}$  nanoflake interfaces for  $\text{O}_2$  activation and boosting NO photo-oxidation. *Appl Catal B: Environ* **2022**;302:120876.
20. Liu YB, Zhu GQ, Gao JZ, Hojamberdiev M, Zhu RL, Wei XM, Guo QM, Liu P. Enhanced photocatalytic activity of  $\text{Bi}_4\text{Ti}_3\text{O}_{12}$  nanosheets by  $\text{Fe}^{3+}$ -doping and the addition of Au nanoparticles: photodegradation of phenol and bisphenol A. *Appl Catal B Environ* **2017**;200:72.
21. Chen ZW, Jiang H, Jin WL, Shi CK. Enhanced photocatalytic performance over  $\text{Bi}_4\text{Ti}_3\text{O}_{12}$  nanosheets with controllable size and exposed 0 0 1 facets for rhodamine B degradation. *Appl Catal B Environ* **2016**;180:698.
22. Yu HJ, Chen F, Li XW, Huang HW, Zhang QY, Su SQ, Wang KY, Mao EY, Mei B, Mul G, Ma TY, Zhang YH. Synergy of ferroelectric polarization and oxygen vacancy to promote  $\text{CO}_2$  photoreduction. *Nat Commun* **2021**;12:4594.
23. Wang XY, Wang YS, Gao MC, Shen JN, Pu XP, Zhang ZZ, Lin HX, Wang XX.  $\text{BiVO}_4/\text{Bi}_4\text{Ti}_3\text{O}_{12}$  heterojunction enabling efficient photocatalytic reduction of  $\text{CO}_2$  with  $\text{H}_2\text{O}$  to  $\text{CH}_3\text{OH}$  and  $\text{CO}$ . *Appl Catal B Environ* **2020**;270:118876.
24. Mohammadi AV, Rosen J, Gogotsi Y. The world of two-dimensional carbides and nitrides (MXenes). *Science* **2021**;372:1165.
25. Li YZ, Zhang XT. Electrically conductive, optically responsive, and highly orientated  $\text{Ti}_3\text{C}_2\text{T}_x$  MXene aerogel fibers. *Adv Funct Mater* **2022**;32:2107767.
26. Seyedin S, Uzun S, Levitt A, Anasori B, Dion G, Gogotsi Y, Razal JM. MXene composite and coaxial fibers with high stretchability and conductivity for wearable strain sensing textiles. *Adv Funct Mater* **2020**;30:1910504.
27. Ding JX, Zhang J, Li JN, Li D, Xiao CS, Xiao HH, Yang HH, Zhuang XL, Chen XS. Electrospun polymer biomaterials. *Prog Polym Sci* **2019**;90:1.
28. Zhang X, Lv SS, Lu XC, Yu H, Huang T, Zhang QH, Zhu MF. Synergistic enhancement of coaxial nanofiber-based triboelectric nanogenerator through dielectric and dispersity modulation. *Nano Energy* **2020**;75:104894.
29. Xue JJ, Wu T, Dai YQ, Xia YN. Electrospinning and electrospun nanofibers: methods, materials, and applications. *Chem Rev* **2019**;119:5298.
30. Chen HY, Zhou LL, Fang Z, Wang SZ, Yang T, Zhu LP, Hou XM, Wang HL, Wang ZL. Piezoelectric nanogenerator based on in situ growth all-inorganic  $\text{CsPbBr}_3$  perovskite nanocrystals in PVDF fibers with long-term stability. *Adv Funct Mater* **2021**;31:2011073.
31. Lu LJ, Ding WQ, Liu JQ, Yang B. Flexible PVDF based piezoelectric nanogenerators. *Nano Energy* **2020**;78:105251.
32. Sharma A, Panwar V, Mondal B, Prasher D, Bera MK, Thomas J, Kumar A, Kamboj N, Mandal D, Ghosh D. Electrical stimulation induced by a piezo-driven triboelectric nanogenerator and electroactive hydrogel composite, accelerate wound repair. *Nano Energy* **2022**;99:107419.
33. Zhang XW, Liang YY, Ni CJ, Li YJ. Anti-biofouling microfiltration membranes based on 1-vinyl-3-butylimidazolium chloride grafted PVDF with improved bactericidal properties and vitro biocompatibility. *Mater Sci Eng C* **2021**;118:111411.
34. Sun J, Fan Y, Ye W, Tian LM, Niu SC, Ming WH, Zhao J, Ren LQ. Near-infrared light triggered photodynamic and nitric oxide synergistic antibacterial nanocomposite membrane. *Chem Eng J* **2021**;417:128049.
35. Liu YT, Zhang P, Sun N, Anasori B, Zhu QZ, Liu H, Gogotsi Y, Xu B. Self-assembly of transition metal oxide nanostructures on MXene nanosheets for fast and stable lithium storage. *Adv Mater* **2018**;30:1707334.
36. Yang LY, Cui J, Zhang L, Xu XR, Chen X, Sun DP. A moisture-driven actuator based on polydopamine-modified MXene/bacterial cellulose nanofiber composite film. *Adv Funct Mater* **2021**;31:2101378.
37. Hou TT, Luo QQ, Li Q, Zu HL, Cui PX, Chen SW, Lin Y, Chen JJ, Zheng XS, Zhu WK, Liang SQ, Yang JL, Wang LB. Modulating oxygen coverage of  $\text{Ti}_3\text{C}_2\text{T}_x$  MXenes to boost catalytic activity for  $\text{HCOOH}$  dehydrogenation. *Nat Commun* **2020**;11:4251.
38. Liu LZ, Huang HW, Chen ZS, Yu HJ, Wang KY, Huang JD, Yu H, Zhang YH. Synergistic polarization engineering on bulk and surface for boosting  $\text{CO}_2$  photoreduction. *Angew Chem Int Ed Engl* **2021**;60:18303.
39. Li R, Ma XY, Li JM, Cao J, Gao HZ, Li TS, Zhang XY, Wang LC, Zhang QH, Wang G, Hou CY, Li YG, Palacios T, Lin YX, Wang HZ, Ling X. Flexible and high-performance electrochromic devices enabled by self-assembled 2D  $\text{TiO}_2/\text{MXene}$  heterostructures. *Nat Commun* **2021**;12:1587.
40. Sarycheva A, Gogotsi Y. Raman spectroscopy analysis of the structure and surface chemistry of  $\text{Ti}_3\text{C}_2\text{T}_x$  MXene. *Chem Mater* **2020**;32:3480.
41. Liu LZ, Huang HW, Chen F, Yu HJ, Tian N, Zhang YH, Zhang TR. Cooperation of oxygen vacancies and 2D ultrathin structure promoting  $\text{CO}_2$  photoreduction performance of  $\text{Bi}_4\text{Ti}_3\text{O}_{12}$ . *Sci Bull* **2020**;65:934.

42. Li JF, Li ZY, Liu XM, Li CY, Zheng YF, Yeung KWK, Cui ZD, Liang YQ, Zhu SL, Hu WB, Qi YJ, Zhang TJ, Wang XB, Wu SL. Interfacial engineering of  $\text{Bi}_2\text{S}_3/\text{Ti}_3\text{C}_2\text{T}_x$  MXene based on work function for rapid photo-excited bacteria-killing. *Nat Commun* **2021**;12:1224.
43. Ran JR, Gao GP, Li FT, Ma TY, Du AJ, Qiao SZ.  $\text{Ti}_3\text{C}_2$  MXene co-catalyst on metal sulfide photo-absorbers for enhanced visible-light photocatalytic hydrogen production. *Nat Commun* **2017**;8:13907.
44. Wu XH, Wang JH, Wang ZY, Sun F, Liu YZ, Wu KF, Meng XY, Qiu JS. Boosting the electrocatalysis of MXenes by plasmon-induced thermalization and hot-electron injection. *Angew Chem Int Ed Engl* **2021**;60:9416.
45. Hsu PC, Song AY, Catrysse PB, Liu C, Peng YC, Xie J, Fan SH, Cui Y. Radiative human body cooling by nanoporous polyethylene textile. *Science* **2016**;353:6303.
46. Li ZJ, Cheng BW, Ju JG, Kang WM, Liu Y. Development of a novel multi-scale structured superhydrophobic nanofiber membrane with enhanced thermal efficiency and high flux for membrane distillation. *Desalination* **2021**;501:114834.
47. Deka S, Devi MB, Khan MR, Keerthana, Venimadhav A, Choudhury B. Piezo-photocatalytic and photocatalytic bismuth vanadate nanorods with antibacterial property. *ACS Appl Nano Mater* **2022**;5:10724.
48. Jia YN, Zhan SH, Ma SL, Zhou QX. Fabrication of  $\text{TiO}_2\text{-Bi}_2\text{WO}_6$  binanosheet for enhanced solar photocatalytic disinfection of *E. coli*: insights on the mechanism. *ACS Appl Mater Interfaces* **2016**;8:6841.
49. Wang XL, Li ZH, Zhang Y, Li QL, Du H, Liu F, Zhang XL, Mu HB, Duan JY. Enhanced photocatalytic antibacterial and

degradation performance by p–n–p type  $\text{CoFe}_2\text{O}_4/\text{CoFe}_2\text{S}_4/\text{MgBi}_2\text{O}_6$  photocatalyst under visible light irradiation. *Chem Eng J* **2022**;429:132270.

**Publisher's Note** Springer Nature remains neutral with regard to jurisdictional claims in published maps and institutional affiliations.

Springer Nature or its licensor (e.g. a society or other partner) holds exclusive rights to this article under a publishing agreement with the author(s) or other rightsholder(s); author self-archiving of the accepted manuscript version of this article is solely governed by the terms of such publishing agreement and applicable law.



**Zhiying Wang** obtained her B.E. from Hebei University of Technology in 2020, majoring in Metal Materials Engineering. She is studying for a master's degree at Tianjin University, majoring in materials science under the guidance of Prof. Shuilin Wu. Her current research interests focus on antibacterial biomaterials.